Peierls-Nabarro model for dislocations in MgSiO3 post-perovskite calculated at 120 GPa from first principles

Ph. Carrez, D. Ferré, P Cordier

Peierls-Nabarro model for dislocations in MgSiO3 post-perovskite calculated at 120 GPa from first principles

Journal:	*Philosophical Magazine & Philosophical Magazine Letters*
Manuscript ID:	TPHM-06-Dec-0476.R2
Journal Selection:	Philosophical Magazine
Date Submitted by the Author:	07-Feb-2007
Complete List of Authors:	Carrez, Ph.; Université des Sciences et Technologies de Lille, Laboratoire de Structure et Propriétés de l Etat Solide Ferré, D.; Université des Sciences et Technologies de Lille, Laboratoire de Structure et Propriétés de l Etat Solide Cordier, P; Université des Sciences et Technologies de Lille, Laboratoire de Structure et Propriétés de l Etat Solide
Keywords:	computer modelling, crystal defects, deformation mechanisms, dislocations, geological materials
Keywords (user supplied):	Peierls-Nabarro model

Peierls-Nabarro model for dislocations in $MgSiO_3$ post-perovskite calculated at 120 GPa from first principles

Ph. Carrez, D. Ferré and P. Cordier

Laboratoire de Structure et Propriétés de l'Etat Solide - UMR CNRS 8008
Université des Sciences et Technologies de Lille
Cite Scientifique, Bat C6
59655 Villeneuve d'Ascq, France

Submitted to Philosophical Magazine
Revised 2

[1]Phone :+33-320-336167 - Fax: +33-320-436591 - E-mail: philippe.carrez@univ-lille1.fr
[1]Phone :+33-320-434778 - Fax: +33-320-436591 - E-mail: denise.ferre@univ-lille1.fr
[1]Phone :+33-320-434341 - Fax: +33-320-436591 - E-mail: patrick.cordier@univ-lille1.fr

ca. 5200 words

ABSTRACT:

We present here the first numerical modelling of dislocations in $MgSiO_3$ post-perovskite at 120 GPa. The dislocation core structures and properties are calculated through the Peierls-Nabarro model using the Generalized Stacking Fault (GSF) results as a starting model. The GSF are determined from first-principle calculations using the VASP code. The dislocation properties such as planar core spreading and Peierls stresses are determined for the following slip systems: [100](010), [100](001), [100](011), [001](010), [001](110), [001](100), [010](100), [010](001), ½[110](001) and ½[110]($\bar{1}$10). Our results confirm that the $MgSiO_3$ post-perovskite is a very anisotropic phase with a plasticity dominated by dislocation glide in the (010) plane.

Key words:

$MgSiO_3$ post-perovskite, deformation mechanisms, dislocations, slip systems, first-principle calculations, Peierls-Nabarro model

§1. INTRODUCTION

The boundary between the Earth's mantle (made of solid rocks) and the liquid core (the core-mantle boundary (CMB) also called D" layer on the mantle side and located at ca. 2900 km depth) is the largest density interface within the Earth's interior. It is characterized by localized regions of anisotropic splitting of shear waves [1-4]. The magnitude of seismic anisotropy shows very strong lateral variations and reveal a complex structure. Several structures can account for the seismic observations. Among them it has been suggested that, as in the upper mantle, seismic anisotropy in D" could arise from lattice-preferred orientations (LPO) of elastically anisotropic minerals caused by plastic deformation [5]. In this context, the recent discovery of a new phase of $MgSiO_3$ [6-8] stable at the P, T conditions of the CMB has attracted a lot of attention. This new phase, called post-perovskite, exhibits an orthorhombic symmetry (space group n°63: Cmcm) with a = 2.456 Å, b = 8.042 Å and c = 6.093 Å [9]. This structure, which exhibits octahedral layers parallel to {010}, appears very anisotropic from the structural point of view (see figure 1). This characteristics has been very early related (at least qualitatively) to the strong seismic anisotropy of the D" layer [7]. Further analysis call for the precise description of the LPO in post-perovskite, i.e. for the knowledge of slip systems and plastic shear anisotropy in this structure.

The post-perovskite phase of $MgSiO_3$ is only stable in the lowermost 150 km of the mantle, i.e. at conditions in excess 120 GPa and 2000 K. Direct experimental determination of the dislocations and slip systems is thus presently out of reach in this mineral. The slip systems depend intimately on the structure and bonding of materials. The usual concept of close-packed planes introduced in metals appears insufficient to predict glide planes in minerals. Alternatively, it has been shown recently in olivine [10], MgO [11] and Mg_2SiO_4 ringwoodite [12] that the concept of generalised stacking faults (GSF) is able to capture very efficiently the essential features of plastic shear anisotropy. Moreover, GSF energies lead to reliable values for the restoring forces close to the core of a dislocations core. Following the seminal work of Vitek and co-workers, several studies have shown that GSF energies can be used as an input in the Peierls-Nabarro (PN) model to provide reasonable models of dislocations in case of planar cores [13-15].

In this study, we use the first-principles to calculate the GSF energies along the Burgers vector direction for several potential slip systems in the post-perovskite structure at 120 GPa. Dislocation properties are then derived using the framework of the PN model. This

model, which is summarized in the first part, allows to calculate dislocation cores and the possible dissociations assuming collinear dissociations. It leads also to the determination of the Peierls stress (σ_p). This information is finally used to infer the possible slip system of the post-perovskite phase.

§2. THE PEIERLS-NABARRO MODEL

The original Peierls Nabarro (PN) model [16, 17] represents a useful and efficient approach to calculate the core properties of dislocations [18-20] based on the assumption of a planar core [21]. It has been shown to apply to a wide range of materials [20, 22-25, 11]. The purpose of this section is to briefly review the relevant aspects of the PN model for application to dislocations in $MgSiO_3$ post-perovskite at 120 GPa.

The PN model assumes that the misfit region of inelastic displacement is restricted to the glide plane, whereas linear elasticity applies far from it. The dislocation corresponds to a continuous distribution of shear S(x) along the glide plane (x is the coordinate along the displacement direction of the dislocation in the glide plane). S(x) represents the disregistry across the glide plane and the stress generated by such a displacement can be represented by a continuous distribution of infinitesimal dislocations with density $\rho(x)$ for which the total summation is equal to the Burgers vector b. The restoring force F acting between atoms on either sides of the interface is balanced by the resultant stress of the distribution leading to the well-known Peierls Nabarro (PN) equation:

$$\frac{K}{2\pi}\int_{-\infty}^{+\infty}\frac{1}{x-x'}\left[\frac{dS(x')}{dx'}\right]dx' = \frac{K}{2\pi}\int_{-\infty}^{+\infty}\frac{\rho(x')}{x-x'}dx' = F(S(x)) \qquad (1)$$

where K, the energy coefficient is function of the dislocation character. This coefficient can be calculated within the frame of the Stroh theory [26] to take anisotropic elasticity into account. As largely developed by Joos & Duesbery [19], an analytical solution of the PN equation can be found by introducing a sinusoidal restoring force:

$$F(S(x)) = \tau^{\max}\sin\left(\frac{2\pi S(x)}{b}\right) \qquad (2)$$

where b is the dislocation Burgers vector and τ^{max} is the ideal shear strength (ISS) which is defined as the "maximum resolved shear stress that an ideal, perfect crystal can suffer without plastically deforming" [27]. Incorporating this expression in the PN equation leads to a classic solution for the disregistry function:

$$S(x) = \frac{b}{\pi}\tan^{-1}\frac{x}{\zeta} + \frac{b}{2} \qquad (3)$$

where $\zeta = \frac{Kb}{4\pi\tau^{max}}$ represents the half-width of the ρ(x) dislocation distribution. One can easily check that the disregistry across the glide plane S(x) verifies the limits, S(x) = 0 when x → -∞ (far from the dislocation), S(x) = b when x→ +∞ (on the other side) and the summation of S(x) over the whole space is equal to the Burgers vector b of the dislocation.

In order to obtain the misfit energy corresponding to the Peierls dislocation and to determine the Peierls stress, the sum of the local misfit energy has to be done at the position of atoms rows parallel to the dislocation line. Indeed, the PN equation holds for an elastic continuous medium whereas S(x) can only be defined where an atomic plane is present (e.g. [26, 28]). The misfit energy can be thus considered as the sum of misfit energies between pairs of atomic planes (e.g. [29, 19]) and can be written as

$$W(u) = \sum_{m=-\infty}^{+\infty} \gamma(S(ma' - u)) \cdot a' \tag{4}$$

where a' is the periodicity of W, taken as the shortest distance between two equivalent atomic rows in the direction of the dislocation's displacement. The Peierls stress is then given by:

$$\sigma_P = \max\left\{\frac{1}{b}\frac{dW(u)}{du}\right\} \tag{5}$$

In order to solve the misfit energy function analytically, Joos & Duesbery [19] introduced a dimensionless parameter Γ= ζ/a'. Then, some simple formulas can be derived for the extreme cases of very narrow (Γ<<1) and widely spread (Γ>>1) dislocations:

$$\sigma_p(\Gamma << 1) = \frac{3\sqrt{3}}{8}\tau^{max}\frac{a'}{\pi\zeta} \tag{6}$$

and

$$\sigma_p(\Gamma >> 1) = \frac{Kb}{a'}\exp\left(\frac{-2\pi\zeta}{a'}\right) \tag{7}$$

The range of the limits was recently extended to the case 0.2<Γ<0.5 where equation (7) has to be modified to take into account an exponential correction term [30].

The analytical solution presented above can be applied in case of a sinusoidal restoring force and with the knowledge of the ISS value. As demonstrated by Vitek [31], the restoring force introduced in the PN model is simply the gradient of the so-called generalised stacking fault γ:

$$\vec{F}(S) = -\overrightarrow{grad}\gamma(S) \tag{8}$$

Thus the aim of the following is to determine from first principles the GSF for potential slip systems in post-perovskite and then to use the GSF results as input of a PN model.

§3. AB-INITIO CALCULATIONS

3.1. Technique

Calculations were performed using the *ab initio* total-energy calculation package VASP (Vienna Ab Initio Package) developed by Kresse and Hafner [32-35]. This code is based on the first-principles density functional theory and solves the effective one-electron Hamiltonian involving a functional of the electron density to describe the exchange-correlation potential. It gives access to the total energy of a periodic system with, as a single input, the atomic numbers of atoms. Computational efficiency is achieved using a plane wave basis set for the expansion of the single electron wave functions and fast numerical algorithms to perform self-consistent calculations [36]. Within this scheme, we used the Generalised Gradient Approximation (GGA) derived by Perdrew & Wang [37] and the all-electron Projector Augmented-Wave (PAW) method as implanted in the VASP code [38, 36]. Using this assumption, the outmost core radius for the Mg, Si and O atoms are 2, 1.9 and 1.52 a.u respectively. Computation convergence is achieved in all simulations by using a single energy cut-off value of 600 eV for the plane wave expansion. The first Brillouin zone is sampled using a Monkhorst-Pack grid [39] adapted for each supercell geometry in order to achieve the full energy convergence. As an example, $MgSiO_3$ post-perovskite unit cell calculations were performed using a 6x4x4 grid with a convergence energy less than 0.08 meV for an external pressure of 120 GPa.

3.2. Structure and elasticity

The $MgSiO_3$ post-perovskite crystallographic structure was optimised (full relaxation of the cell parameters and of the atomic positions within the cell) under a pressure of 120 GPa. The calculated cell parameters are a = 2.474 Å, b = 8.112 Å and c = 6.139 Å under these conditions. These values are in good agreement with the previous results of post-perovskite cell parameters either determined using LDA [9] or GGA approximation [7]. To determine the athermal elastic constants, the equilibrium cell was strained using adapted deformations, which were kept lower than 0.02. To account for the pressure effect, the energy was calculated along the lines described by Barron & Klein [40] to incorporate the work of pressure. The elastic constants are then determined from the fit of the total energy versus

strain by a second order polynomial (see [12] for details). The results of the nine elastic constants are presented Table 1. Again, our results agree well with previous published values (e.g. GGA results of Oganov & Ono [7]) and reveal the anisotropy of the $MgSiO_3$ post-perovskite phase with a C_{22} modulus significantly lower than C_{11} and C_{33}. The energy coefficient $K(\theta)$ for every dislocation of interest are finally calculated using our C_{ij} (Table 1) as an input of the DisDi software [41] which is based on the Stroh theory.

3.3. Generalised stacking faults

Calculating a GSF for a given slip system requires a supercell with an adapted geometry. The supercell is built on a cartesian reference frame defined by the normal to the stacking fault plane (located in the middle of the supercell) and by the shear direction. The last direction is then defined as the cross product of the two previous. The supercells are built with only one stacking fault and it is necessary to add a vacuum buffer parallel to the stacking plane. A 6 Å-thick vacuum layer and about five atomic layers on both sides of the stacking fault are sufficient to guarantee energy accuracy better than 0.01 % with a 6x2x4 Monkhorst-Pack grid.

The post-perovskite structure is based on an orthorhombic C-lattice, which means that potential Burgers vectors can be [100], [010], [001] or ½<110>. The five supercells used in this study are presented Figure 2. They allowed us to investigate the following slip systems: [100](010), [100](001), [100](011), [001](010), [001](110), [001](100), [010](100), [010](001), ½[110](001) and ½[110]($\bar{1}$10). The GSF are calculated by imposing a given shear displacement value to the upper part of the supercell. Atoms close to the vacuum layer are maintained fixed to mimic the action of the surrounding bulk atoms in the direction normal to the shear plane and to preserve pressure. These fixed atoms are represented as dark spheres on figure 2. As for the other atoms, shear is imposed by fixing the coordinates in the shear direction. They are however free to relax in the two other directions. The only exception of these general relaxation conditions is for ½[110](001). As the structure is orthorhombic, there is no low index crystallographic direction perpendicular to [110]. The supercell is thus based on [100] and [010] directions in the basal plane and shear is imposed by fixing the two coordinates in the basal plane with, as a consequence, only a vertical degree of freedom.

§4. Generalised Stacking Faults (GSF) and Ideal Shear Stresses (ISS)

The GSF excess energies γ calculated for the whole set of shear configurations reported in the previous section are presented on figure 3. One case ([100] shear on (011)) indeed shows a purely sinusoidal barrier. Most GSF significantly deviate from this ideal case, some of them showing more complex shapes like for a [010] shear in (100). The shape of the GSF reflects the symmetries of the structure in the glide plane. Several systems show a camel hump shape. As for the shapes, the heights of the GSF vary significantly as reported in table 2. The highest energy barrier corresponds to the [010](100) system whereas the lowest barriers correspond to the three [100] shears (Table 2). This result may not be surprising when one considers that [010] is the largest shear vector (8.11 Å) whereas (001) planes have the lowest interplanar distance (2.47 Å). Shear along [100] exhibit very similar GSF on (011) or (001). This can be understood by examining the atomic configurations in those planes. In both cases, the SiO_6 tetrahedra exhibit the same configurations and are sheared along the smallest lattice repeat. For the ½[110](001) slip system, we have already pointed out that the GSF is calculated with only vertical relaxations. Therefore, the GSF may slightly overestimate the energy barrier when compared to the other systems. For the camel hump GSF's, a local energy minimum is found at 50% of shear and can be viewed as a stacking fault energy (SFE) as listed in table 2. The lowest SFE's are found for [001](010) and [010](001) slip systems.

The shear resistance of a given slip system cannot be inferred simply from the maximum GSF energies γ^{max} as the magnitude of the shear vectors will play a role as well. This is particularly important in the post-perovskite structure which exhibits very contrasted lattice vectors moduli. The simplest approach to infer the relative resistance of the slip systems is to determine the ideal shear stress τ^{max} introduced above [13, 42-44]. The values of τ^{max} are presented in Table 2. They do not simply correlate to γ^{max}, reflecting the influence of the shear vector lengths as suggested above. The resistance to plastic shear is lowest for all three [100] shears (corresponding to the shortest lattice repeat) whatever the glide plane, whereas some of the hardest shear configurations are obviously found along [010] (largest cell parameter). Normalising τ^{max} by the relevant shear modulus allows to remove any possible contribution of elastic anisotropy and enables comparison with other structures. Most metals yield values in the range 0.09-0.17μ [27, 45-47] which compare well with those found in Mg_2SiO_4 olivine [10] or ringwoodite [12]. The normalised ISS for [100] shear are very

comparable to the values observed in those silicates (which are stable at lower pressures) whereas other slip systems face significantly larger intrinsic shear resistances.

§5 APPLICATION OF THE PN MODEL TO POST-PEROVSKITE

In this section, the PN model is applied to the case of post-perovskite for the [100](010), [100](001), [100](011), [001](010), [001](110), [001](100), [010](100), [010](001), ½[110](001) and ½[110](-110) slip systems. The case of unsplit and split dislocations will be presented successively.

5.1. Unsplit dislocations

The analytic formula of Joos and Duesbery [19] can be applied directly to the case of the [100](011) dislocations where the restoring force F can be fitted with a simple sine function. In order to apply the PN model, one needs to know the periodicity *a'*. For [100](011) dislocations, screw segments move along a [01-1] direction whereas edge segments move along [100] (so *a'* = 10.16 and 2.47 Å for screw and edge segments respectively, see Table 3). We can then determine the half-width of the dislocation cores using the previous definitions. In case of screw [100](011) dislocations, using τ^{max} = 61.7 GPa, we find ζ_{screw} = 1.03 Å which leads Γ = 0.1 suggesting an extremely narrow core. The Peierls stress is thus 125.7 GPa for [100](011) screw dislocations. The value of σ_p found here is relatively high and may be considered as an upper limit in case of a narrow core. For edge dislocations, ζ_{edge} = 1.56 Å and Γ = 0.6 which corresponds to the second limit with a wider core, the Peierls stress calculated for edge dislocations is 9.3 GPa.

In most cases, the GSF are not purely sinusoidal. The analytical formula cannot be used but the restoring force and disregistry function can still be developed as sine and arctan series [48, 29, 44]. Following the work of Joos et al. [29], we have chosen to look for a disregistry distribution in the dislocation core S(x) represented by:

$$S(x) = \frac{b}{2} + \frac{b}{\pi}\sum_{i=1}^{N} \alpha_i \cdot \arctan\frac{x - x_i}{c_i} \qquad (9)$$

where α_i, x_i and c_i are variational constants. Using the previous disregistry function (equation 9) in the left-hand side of the PN equation gives a trial restoring force (containing the α_i, x_i and c_i parameters). The variational constants α_i, x_i and c_i are obtained from a least square minimisation of the difference between the trial force and the restoring force F derived from our *ab initio* calculations (see [12] for the details of the calculations).

Practically, the restoring force is obtained by derivating the GSF calculated *ab initio* and the disregistry function is developed in an arctan series (to the third order, N=3, found to be sufficient to obtain a continuous dislocation density curve as shown later) in case of a simple (i.e. with one maximum only) energy barrier. Dislocations belonging to the slip systems [100](010), [100](001), ½[110](001) and ½[110](-110) were analysed using this technique. An example of disregistry S(x) and dislocation density ρ(x) is given in figure 4 (case of the [100](010) slip system). As expected, as the restoring force is not purely sinusoidal, the resulting dislocation core profile can be very different from that obtained from the analytical solution (Table 3, see for example, the screw ½[110](001) which is very far from the sinusoidal case. See also Figure 4 with the superposition of the analytical solution to our model). It is a general observation that edge dislocation cores are wider than screw's. Calculations for both edges and screws start from the same GSF but differences arise from the elastic response of the interface and of the lattice. Due to the Poisson ratio, screw components have lower elastic energies and thus, the core is narrower [26]. With the fitted dislocation disregistry, we numerically determine both the misfit energy and the Peierls stress using equation (6) and (7) respectively. The results are also presented in Table 3. The values of σ_p are very sensitive to the half-width of the dislocation and to the periodicity of the crystal in the glide direction. As a consequence, the σ_p values increase when the ratio $\Gamma = \zeta/a'$ decreases.

5.2. The case of split dislocations

A special attention must be given to GSF with multiple maxima because they are likely to describe dissociated dislocations. For instance, some GSF exhibit camel hump shapes ([001](100), [001](110), [001](010), and [010](001)). Applying the same treatment of the variational disregistry function S requires to increase the order of the series to N=6 (in order to reproduce two well-defined partial dislocation densities). Two typical examples of dislocation cores dissociated into partials are presented on figure 5 and 6. They correspond to the [001](110) and [010](001) slip systems. The symmetry of the GSF is reproduced as the two partials dislocation are identical and correspond to a collinear dissociation of the total Burgers vector b into two partials with $b/2$ Burgers vector. The fit of the total restoring force imposes an equilibrium distance between the partials. Table 4 summarises the results of half-width of partials and separation distance between the two partials. For dissociated dislocations, the core profiles result from the interplay between the elastic energy and the stacking fault energy (SFE). As previously noticed for perfect cores, partial screws are generally narrower compared to edges. The difference between screw and edge components is

directly correlated with the elastic energy. However, the separation between the partials depends on the slip system. Some cases can exhibit a strong overlap (see figure 6 or the distances $\Delta\zeta$ in table 4), some do not as shown for [010](001) (Figure 5). The splitting distance is mostly determined by the SFE [28]. Low SFE lead to large dissociations (these data are available from Tables 2 and 4).

For dissociated dislocations, the misfit energy and the Peierls stress are still given by equation (6) and (7). We thus implicitly consider that the two partial dislocations are strongly coupled. Whatever the position of the first partial dislocation in the crystal, our calculations consider the second partial at the position corresponding to the equilibrium distance $\Delta\zeta$. Thus, it is possible that one partial goes up the Peierls barrier whereas the second goes down leading to a minimisation of the total energy and thus sometimes to a strong decrease of the Peierls stress [49, 44]. Result of equation (7) as applied in this study gives access to what usually called the effective Peierls stress that is the stress needed to move the dislocation as a whole and not the stress needed to move only one partial [49, 50].

Finally, the [010](100) slip system, which exhibits a complex GSF, is analyzed with the same procedure but with increasing the series order N (equation 9) to N=9 as a dissociation into more than two partials is suspected. The dislocation density curves corresponding to this slip system are presented on figure 7. The curve shows a continuous distribution of dislocation density which can be viewed as a three-partials decomposition. The splittings for both edge and screw dislocations are symmetrical. This situation is similar to the splitting of dislocations found by Kroupa & Lejcek [48] for ½<111>(110) dislocations in α-Fe. The Peierls stress σ_p for the screw component and for the edge component are 95.5 and 57.3 GPa respectively. Again, these values of σ_p correspond to the stress needed to overcome the Peierls barrier when the whole set of partials are rigidly move without any modification of the core profile [21].

§6. Discussion

The present study is originally motivated by the paramount interest in the post-perovskite phase in order to model the behaviour of the core-mantle boundary. This phase appears also to be of great interest from the fundamental point of view. The field of the

computational modelling approach of dislocations and plasticity is extended here to incorporate a silicate with a complex crystal chemistry. Taking the more simple chemical composition of the post-perovskite phase (pure Mg compound) we need to incorporate three different atomic species: Mg, Si and O. This chemistry gives rise to several kinds of bonds: Mg-O and Si-O, which, under the pressure conditions considered here (120 GPa) corresponds to an octahedral coordination. The interest of $MgSiO_3$ post-perovskite lies in the presence of Mg layers in the (010) plane the importance of which will be discussed below. Correspondingly, the edge-sharing SiO_6 octahedra are located into (010) layers alternating with the Mg layers. What distinguishes also $MgSiO_3$ post-perovskite among high-pressure silicates is that the orthorhombic unit-cell exhibits edges with very different lengths. Combined with the face-centred mode of the Bravais lattice, one finds four potential Burgers vectors spanning a wide range of moduli. This is readily observed on the GSF presented Figure 3. The present study shows that core structures depend mostly on the Burgers vector modulus.

The shortest Burgers vector is [100]: 2.47 Å. [100] dislocations exhibit narrow cores in the range of 1.03-1.16 Å for screws and 1.54-1.88 for edges. The next Burger vectors are ½<110> (4.24 Å). Although their moduli are significantly larger (1.7*a*), their core profiles do not differ significantly to [100] dislocations. Only ½[110] dislocations gliding in $(\bar{1}10)$ exhibit somewhat wider profiles: 1.65 Å for the screws and 2.2 Å for the edges. The situation changes with the [001] dislocations (6.14 Å) which exhibit a tendency for core spreading in their glide planes. The dislocation density profile becomes double-peaked. [001] dislocations tend to dissociate into their glide planes although the cores of the partials still overlap significantly, especially in the (100) and (110) planes. The case of [001](010) must be highlighted. The dislocations need here be considered dissociated, not only because of the limited overlapping of the partials, but also because the partial separation extends over four periods of the Peierls potential. This core structure has serious implications on dislocations mobilities as described below. The largest Burgers vector in $MgSiO_3$ post-perovskite is [010]: 8.11 Å. Dislocations belonging to the [010](001) slip system are widely dissociated with non-overlapping cores extending over several Peierls hills (14 for the screws and 5 for the edges, see Table 4). On the other hand [010] dislocations gliding in (100) exhibit a complex structure with three partials. Dislocation core spreading is a fundamental parameter that controls largely dislocation mobility. The great advantage of the Peierls model is that, beyond providing a topological model for the dislocations cores, it gives an estimate of the mechanical properties

through the stress needed to move the dislocation line at 0K over the distance *a'* (the Peierls stress). The results are described below for each plane.

The presence of alternating Mg and Si layers has immediately attracted attention in a phase supposed to exist in a region of the Earth (the CMB) characterized by a large seismic anisotropy. Intuitively, it has early been speculated that preferential shear would take place along this plane due to weaker bonding. Our results confirm this hypothesis. We show that among the possible slip systems, we find [100] and [001] slip in the (010) plane. However, we find that the easiest slip system does not correspond to [100] slip (which involves the shortest Burgers vector) but to [001] slip in (010) (Table 5). This behaviour is likely to be due to the significant core spreading of [001] dislocations whereas [100] dislocations remain very narrow and hence more difficult to move. Next to this slip system, we find [100](001) (Table 5). Slip in this plane shows several interesting features. [100](001) dislocations exhibit very anisotropic mobilities. Edge segments bears almost no lattice friction (0.3 GPa) contrary to screw segments which need to overcome a larger Peierls stress (47 GPa). It is expected that such behaviour will give rise to fast edge segments producing long straight screw segments the mobility of which will control the mechanical properties. For this reason, we will always consider that the hardest character controls plastic flow. The same behaviour (with one dislocation character bearing little or no lattice friction) is shared by other slip systems in the same plane: ½[110](001) and [010](001). This clearly suggests that a small value of *a'* is a critical parameter in lowering the lattice friction. Indeed, the (001) plane contains the smallest lattice repeat and is face-centred (i.e. the periodicity of the Peierls valley is half of the lattice repeat). Another potential slip system in $MgSiO_3$ post-perovskite is [001](110) with a maximum value of Peierls stress on screw segments of 54 GPa (Table 5). This potential slip system has also the characteristic of exhibiting relatively isotropic loops. Glide in (100) seems to be difficult in any direction. Surprisingly, [010] slip is slightly easier in this plane than [001] slip, probably due to the ability of [010] dislocations to dissociate. Finally, for [100](011) and ½[110](110) slip system, the Peierls stresses for the screw dislocation are found to be the highest and these systems appears difficult to activate.

It is possible to compare Peierls stresses from different materials by normalising σ_p by the shear modulus μ which can be calculated using anisotropic elasticity. This seems relevant in our case as part of the pressure effect will be included in the evolution with pressure of the elastic constants. For $MgSiO_3$ post-perovskite σ_p/μ is in the range 10^{-3}-10^{-2}. Wang [20] has gathered a compilation of experimental σ_p/μ based on yield stress data extrapolated at 0K.

The values calculated for $MgSiO_3$ post-perovskite compare well to covalent materials or to some bcc or hexagonal metals. Finally, there are only limited information available on post-perovskite up to now. Oganov et al. [51] have used a novel simulation technique, first-principles metadynamics, to identify low-energy polytypic stacking-faults involved in the $MgSiO_3$ perovskite - post-perovskite transformation. It is likely indeed that the {110} planes identified in their study is more relevant in the context of phase transformation than in the one of plasticity as our calculations performed on $MgSiO_3$ post-perovskite in its stability field show that slip is not particularly easy on {110}. Similarly, recent deformation experiments performed at room temperature and high-pressure (100-130 GPa) on a structural analogue of post-perovskite with the $MgGeO_3$ composition points to a combination of (100) and (110) slip [52]. Without clearly rejecting a possible glide of dislocations in (100) planes, our calculations show that [001](010), [100](001) and [001](110) are the most relevant slip systems. More precise comparison would require modelling of their compression texture using our prediction for the slip systems (assuming $MgGeO_3$ is a relevant analogue of $MgSiO_3$ in describing the plastic properties of the post-perovskite phase).

Finally, we want to make very clear that the analysis presented above holds only within the framework of the PN model, i.e. for dislocation cores extending within the glide plane. In some cases, dislocations can exhibit three-dimensional core structures which lead to strong lattice frictions (see for instance screw dislocations in bcc metals). Such dislocation cores can be found in certain structures when screw dislocations can spread on several planes simultaneously. This possibility must be considered for [001] screw dislocations which show a strong tendency to spread on (010), (100), (110) and $(1\bar{1}0)$ (in decreasing order). Consequently, one cannot rule out the possibility that [001] screw dislocations exhibit a complex 3D dislocation core. In that case, it is likely that [001] screw dislocations would bear a strong lattice friction and the conclusions presented in Table 5 should be corrected with [100](010) being the easiest slip system. However, it is not possible at this stage to go beyond educated guesses as we are not able to calculate 3D cores with the Peierls model. For that reason, we keep our discussion at the level where reliable calculations can be performed.

§7. Conclusion

We present here a numerical approach of dislocation properties in $MgSiO_3$ post-perovskite based on the Peierls-Nabarro model. The GSF are calculated from the first-principles and used as an input in the model through the restoring forces in the dislocation core.

The potential dislocations in $MgSiO_3$ post-perovskite exhibit Burgers vectors with very different moduli. We show that the tendency for core spreading increases with the modulus of the Burgers vector. Our calculations suggest that [001](010) is the easiest slip systems in $MgSiO_3$ post-perovskite phase under a pressure of 120 GPa provided dislocations exhibit a planar core. The question of a possible 3D extension of the cores of [001] screw dislocations is raised. We show that most dislocations must overcome high lattice frictions. There are some exceptions however since edge [100](001), screw [010](001) as well as 17° ½[110](001) are likely to have very high mobilities (proportional to stress as in fcc metals) at finite temperatures. Plastic slip appears to be very difficult in (100), (011) and in (110) along [110].

ACKNOWLEDGEMENTS

We acknowledge the contribution of S. Effeindzourou for the calculations. This work was supported by CNRS-INSU under the DyETI program. Computational resources have been provided by IDRIS (project # 031685) and CRI-USTL supported by the Fonds Européens de Développement Régional and Région Nord – Pas de Calais.

References:

[1] Kendall, J.-M. and Silver, P. G. 1998. Investigating causes of D" anisotropy. In: The Core-Mantle Boundary Region (edited by Gurnis, M., Wysession, M. E., Knittle, E. & Buffet, B. A.). Geodynamics Series 28. American Geophysical Union, Washington, DC, 97.

[2] Lay, T., Williams, Q. and Garnero, E. J., 1998, Nature, 392, 461.

[3] Wysession, M. E., Lay, T., Revenaugh, J., Williams, Q., Garnero, E. J., Jeanloz, R. and Kellogg, L. H. 1998. The D" discontinuity and its implications. In: The Core-Mantle Boundary Region (edited by Gurnis, M., Wysession, M. E., Knittle, E. & Buffet, B. A.). Geodynamics Series 28. American Geophysical Union, Washington, DC, 273.

[4] Panning, M. and Romanowicz, B., 2004, Science, 303, 351.

[5] Mainprice, D., Barruol, G. and Ben Ismaïl, W. 2000. The seismic anisotropy of the Earth's mantle: from single crystal to polycrystal. In: Earth deep interior: mineral physics and tomography from the atomic scale to the global scale (edited by Karato, S. I.). Geophysical Monograph 117. American Geophysical Union, Washington, D.C., 237.

[6] Murakami, M., Hirose, K., Kawamura, K., Sata, N. and Ohishi, Y., 2004, Science, 304, 834.

[7] Oganov, A. R. and Ono, S., 2004, Nature, 430, 445.

[8] Tsuchiya, T., Tsuchiya, J., Umemoto, K. and Wentzcovitch, R. M., 2004a, *Earth Planet. Sci. Lett.*, **224**, 241.

[9] Itaka, T., Hirose, K., Kawamura, K. and Murakami, M., 2004, Nature, 430, 442.

[10] Durinck, J., Legris, A. and Cordier, P., 2005, Amer Mineral, 90, 1072.

[11] Miranda, C. R. and Scandolo, S., 2005, Comp. Phys. Comm., 169, 24.

[12] Carrez, P., Cordier, P., Mainprice, D. and Tommasi, A., 2006, Eur. J. Mineral., 18, 149.

[13] Vítek, V., 1974, Crystal Lattice Defects, 5, 1.

[14] Vitek, V. and Yamaguchi, M., 1973, J. Phys. F: Met. Phys., 3, 537.

[15] Yamaguchi, M. and Vitek, V., 1973, *J. Phys. F: Met. Phys.*, **3**, 523.

[16] Peierls, R. E., 1940, Proc. Phys. Soc. Lond., 52, 34.

[17] Nabarro, F. R. N., 1947, Proc. Phys. Soc. Lond., 59, 256.

[18] Ren, Q., Joos, B. and Duesbery, M. S., 1995, Phys. Rev. B, 52, 13223.

[19] Joos, B. and Duesbery, M. S., 1997, Phys. Rev. Lett., 78, 266.

[20] Wang, J. N., 1996, Mater. Sci. Eng. A, 206, 259.

[21] Schoeck, G., 2005, Mater. Sci. Eng. A, 400-401, 7.

[22] Bulatov, V. V. and Kaxiras, E., 1997, Phys. Rev. Lett., 78, 4221.

[23] von Sydow, B., Hartford, J. and Wahnström, G., 1999, Comp. Mat. Sci., 15, 367.

[24] Lu, G., Kioussis, N., Bulatov, V. V. and Kaxiras, E., 2000, Phys. Rev. B, 62, 3099.

[25] Lu, G. 2005. The Peierls-Nabarro Model of Dislocations: A venerable theory and its current development. In: Handbook of Materials Modeling. Volume 1: Methods and Models (edited by Yip, S.). Springer, 1.

[26] Hirth, J. P. and Lothe, J., 1982, Theory of dislocations.(New York: John Wiley & Sons, Inc).

[27] Paxton, A. T., Gumbsch, P. and Methfessel, M., 1991, Philos. Mag. Lett., 63, 267.

[28] Schoeck, G., 1999, Philos. Mag. A, 79, 2629.

[29] Joos, B., Ren, Q. and Duesbery, M. S., 1994, Phys. Rev. B, 50, 5890.

[30] Joos, B. and Zhou, J., 2001, Philos. Mag. A, 81, 1329.

[31] Vítek, V., 1968, Phil. Mag., 18, 773.

[32] Kresse, G. and Hafner, J., 1993, Phys. Rev. B, 47, 558.

[33] Kresse, G. and Hafner, J., 1994, Phys. Rev. B, 49, 14251.

[34] Kresse, G. and Hafner, J., 1994, J. Phys.: Condens. Mat., 6, 8245.

[35] Kresse, G. and Furthmüller, J., 1996, Phys. Rev. B, 54, 11169.

[36] Kresse, G. and Furthmüller, J., 1996, Comput. Mat. Sci., 6, 15.

[37] Perdew, J. P. and Wang, Y., 1992, Phys. Rev. B, 45, 13244.

[38] Blöchl, P. E., 1994, Phys. Rev. B, 50, 17953.

[39] Monkhorst, H. J. and Pack, J. D., 1976, Phys. Rev. B, 23, 5048.

[40] Barron, T. H. K. and Klein, M. L., 1965, Proc. Phys. Soc., 85, 523.

[41] Douin, J., Veyssière, P. and Beauchamp, P., 1986, Philos. Mag. A, 54, 375.

[42] Medvedeva, N. I., Mryasov, O. N., Gornostyrev, Y. N., Novikov, D. L. and Freeman, A. J., 1996, Phys. Rev. B, 54, 13506.

[43] Sun, Y. and Kaxiras, E., 1997, Philos. Mag. A, 75, 1117.

[44] Hartford, J., von Sydow, B., Wahnström, G. and Lundqvist, B. I., 1998, Phys. Rev. B, 58, 2487.

[45] Söderlind, P. and Moriarty, J. A., 1998, Phys. Rev. B, 57, 10340.

[46] Roundy, D., Krenn, C. R., Cohen, M. L. and Morris Jr., J. W., 1999, Phys. Rev. Lett., 82, 2713.

[47] Krenn, C. R., Roundy, D., Morris Jr., J. W. and Cohen, M. L., 2001, Materials Sci. Eng. A, 317, 44.

[48] Kroupa, F. and Lejcek, L., 1972, Czechoslovak Journal of Physics, B, 813.

[49] Schoeck, G. and Püschl, W., 1994, Mater. Sci. Eng. A, 189, 61.

[50] Szelestey, P., Patriarca, M. and Kaski, K., 2003, Modelling Simul. Mater. Sci. Eng., 11, 883.

[51] Oganov, A. R., Martonák, R., Laio, A., Raiteri, P. and Parrinello, M., 2005, Nature, 438, 1142.

[52] Merkel, S., Kubo, A., Miyagi, L., Speziale, S., Duffy, T. S., Mao, H.-K. and Wenk, H.-R., 2006, Science, 311, 644.

[53] Tsuchiya, T., Tsuchiya, J., Umemoto, K. and Wentzcovitch, R. M., 2004b, Geophys. Res. Lett., 31, L14603.

Tables :

	C_{11}	C_{22}	C_{33}	C_{12}	C_{13}	C_{23}	C_{44}	C_{55}	C_{66}
This study (GGA)	1225	928	1211	409	328	484	281	260	404
Oganov & Ono [7] (GGA)	1252	929	1233	414	325	478	277	266	408
Tsuchiya et al. [53] (LDA)	1308	968	1298	444	343	507	295	278	439
Itaka et al. [9] (LDA)	1270	937	1264	425	329	493	291	264	412

Table 1: Elastic constants of $MgSiO_3$ post-perovskite calculated in this study at 120 GPa compared to other results available in the literature and calculated at the same pressure (including LDA calculations). All elastic constants are in GPa.

Slip System	γ^{max} (J/m^2)	SFE (J/m^2)	τ^{max} (GPa)	τ^{max}/μ
[100](010)	5.55	-	71.7	0.17
[100](011)	4.91	-	61.7	0.21
[100](001)	4.86	-	61.8	0.23
½[110](001)	16.23	-	120.0	0.43
½[110](-110)	14.44	-	133.4	0.36
[001](100)	11.66	9.01	107.1	0.41
[001](110)	11.42	10.14	101.6	0.39
[001](010)	7.50	4.95	78.0	0.28
[010](100)	21.02	-	115.8	0.28
[010](001)	18.11	4.89	131.2	0.47

Table 2: Results of GSF calculations. γ^{max} corresponds to the maximum of the GSF curve. In case of camel hump shape, SFE represents the Stacking Fault Energy i.e the energy value for a *b*/2 shear. The maximum value of the restoring force is given as τ^{max}. It is also presented after being normalised by the shear modulus μ (μ was calculated using anisotropic elasticity from the elastic constant given in Table 1).

	Screw					Edge				
	a' **(Å)**	**K*b*/4πτ^{max} (Å)**	**ζ (Å)**	**ΔW (eV/Å)**	**σ_p (GPa)**	***a'*** **(Å)**	**K*b*/4πτ^{max} (Å)**	**ζ (Å)**	**ΔW (eV/Å)**	**σ_p (GPa)**
[100](010)	6.14	0.89	1.16	1.89	86.9	2.47	1.43	1.88	0.05	4.2
[100](011)	10.16	1.03	1.03	2.90	125.7	2.47	1.56	1.56	0.11	9.3
[100](001)	4.05	1.03	1.06	0.82	47.3	1.24	1.49	1.54	0.002	0.3
½[110](001)*	1.24	0.97	1.23	0.02	1.8	4.05	1.07	1.39	2.52	76.7
½[110](-110)	6.14	0.82	1.65	5.09	154.6	4.24	1.16	2.2	1.42	46.2

Table 3: Results of the Peierls-Nabarro model applied to the five slip systems [100](010), [100](011), [100](001), ½[110](001) and ½[110](-110). *a'* is the periodicity of the Peierls valley. K*b*/4πτ^{max} corresponds to the half width of dislocation core as defined in the analytical solution of the PN equation whereas ζ is the half width of dislocation core deduced from the numerical solution of the PN equation. ΔW Corresponds to the Peierls energy barrier and σ_p is the calculated Peierls stress needed to overcome the energy barrier.

*In case of the ½[110](001) slip system, values are presented for the following mixed characters: θ = 17° in the "Screw" column and θ = 83° in the "Edge" column (θ is the angle between the Burgers vector and the dislocation line).

	screw					edge				
	a' **(Å)**	**ζ (Å)**	**Δζ (Å)** ***(a')***	**ΔW (eV/Å)**	**σ_p (GPa)**	***a'*** **(Å)**	**ζ (Å)**	**Δζ (Å)** ***(a')***	**ΔW (eV/Å)**	**σ_p (GPa)**
[001](100)	8.11	1.11	5.27 (0.65)	3.81	99.3	6.14	2.09	9.08 (1.48)	2.42	37.8
[001](110)	4.24	1.41	4.75 (1.12)	2.46	54.4	6.14	2.17	8.44 (1.37)	2.44	35.5
[001](010)	2.47	1.12	9.85 (3.99)	0.54	18.5	6.14	1.86	16.15 (2.63)	0.65	12.2
[010](001)	1.24	1.16	17.45 (14.07)	0.002	0.1	4.05	1.44	19.72 (4.87)	4.94	75.8
[010](100)*	6.14	ζ_1=1.65 ζ_2=1.29	11.60 (3.78)	6.3	95.5	8.10	ζ_1=1.80 ζ_2=1.30	13.36 (1.65)	4.30	57.3

Table 4: Results of the Peierls-Nabarro model for dissociated dislocations belonging to slip systems [001](100), [001](110), [001](010), [010](001) and [010](100). Here, ζ corresponds to the half width of a partial dislocation and Δζ is the equilibrium distance between the two partials expressed in Å and as a function of the periodicity *a'*. Δζ is the equilibrium distance between the two partials.

For the [010](100) slip system, the values of ζ are presented for the central dislocation density (ζ_1) and for the outer partials (ζ_2).

Slip system	Peierls stress for screw dislocations (GPa)	Peierls stress for edge dislocations (GPa)	Maximum Peierls stress (GPa)	Peierls stress normalised to the easiest slip system
[001](010)	18.5	12.2	18.5	1
[100](001)	47 .3	0.3	47.3	2.6
[001](110)	54.4	35.5	54.4	2.9
½[110](001)	1.8	76.7	76.7	4.1
[010](001)	0.1	75.8	75.8	4.1
[100](010)	86.9	4.2	86.9	4.7
[010](100)	95.5	57.3	96.5	5.2
[001](100)	99.3	37.8	99.3	5.4
[100](011)	125.7	9.3	125.7	6.8
½[110](110)	154.6	46.2	154.6	8.4

Table 5: Summary of the Peierls stresses and comparison of the various slip systems based on the hardest dislocation character. The maximum Peierls stress is the maximum value between the screw and edge characters assuming that the slowest dislocation character will control plastic deformation.

Figure captions:

Figure 1: $MgSiO_3$ post-perovskite structure. SiO_6 octahedrons are displayed in light grey. The anisotropy of the structure is evidenced with SiO_6 layers stacked along the b direction.

Figure 2: Supercells used in this study to calculate the GSF. For all supercells, light grey spheres correspond to Mg atoms, dark grey spheres correspond to O atoms and Si atoms are represented as small black spheres. Atoms close to the surfaces are maintained fixed during calculations and are shown in black.

a) (010) glide
b) (110) glide
c) (001) glide
d) (011) glide
e) (100) glide

Figure 3: Generalised stacking faults calculated in this study. The GSF are displayed against a shear displacement vector $\boldsymbol{u}$ rescaled in such a way that $b/2$ shear corresponds to $\boldsymbol{u}=0$ in order to compare the different slip systems.

Figure 4: Disregistry function S (dashed line) and dislocation density ρ plotted against the distance of the dislocation core for dislocations belonging to the [100](010) slip system. (a) screw dislocation. (b) edge dislocation. The cross symbols correspond to dislocation densities determined using the analytical solution presented in §2.

Figure 5 : Disregistry S (dashed line) and dislocation density ρ plotted against the distance of the dislocation core for [010](001) slip system. (a) screw dislocation. (b) edge dislocation. The dislocations appear to be dissociated into two collinear partials with no overlap between the two partial dislocation densities.

Figure 6 : Disregistry S (dashed line) and dislocation density ρ plotted against the distance of the dislocation core for [001](110) slip system. (a) screw dislocation. (b) edge dislocation.

The dislocations appear to be dissociated into partials for both screw and edge components. The equilibrium distance between the two partial is significantly small (close to one periodicity of the Peierls barrier) with a strong interaction between the partials

Figure 7 : Disregistry S (dashed line) and dislocation density ρ plotted against the distance of the dislocation core for [010](100) slip system. (a) screw dislocation. (b) edge dislocation. For both screw and edge components, the dislocation dissociates into three partials.

Figures

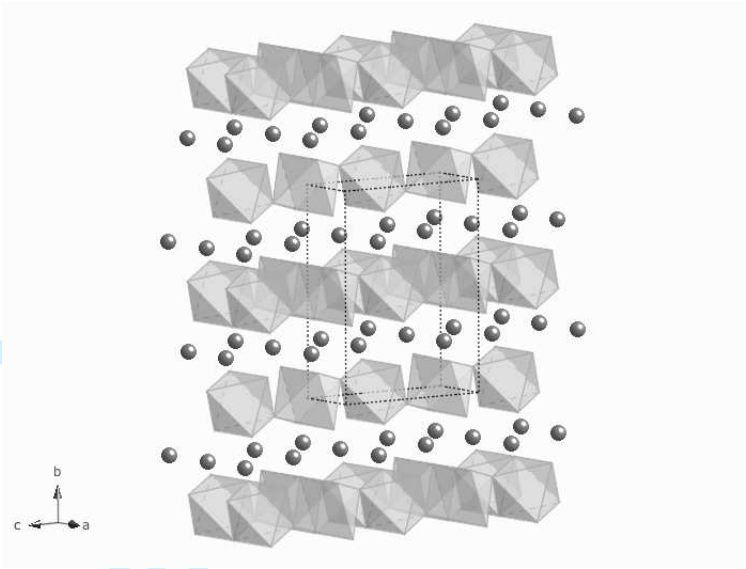

Figure 1

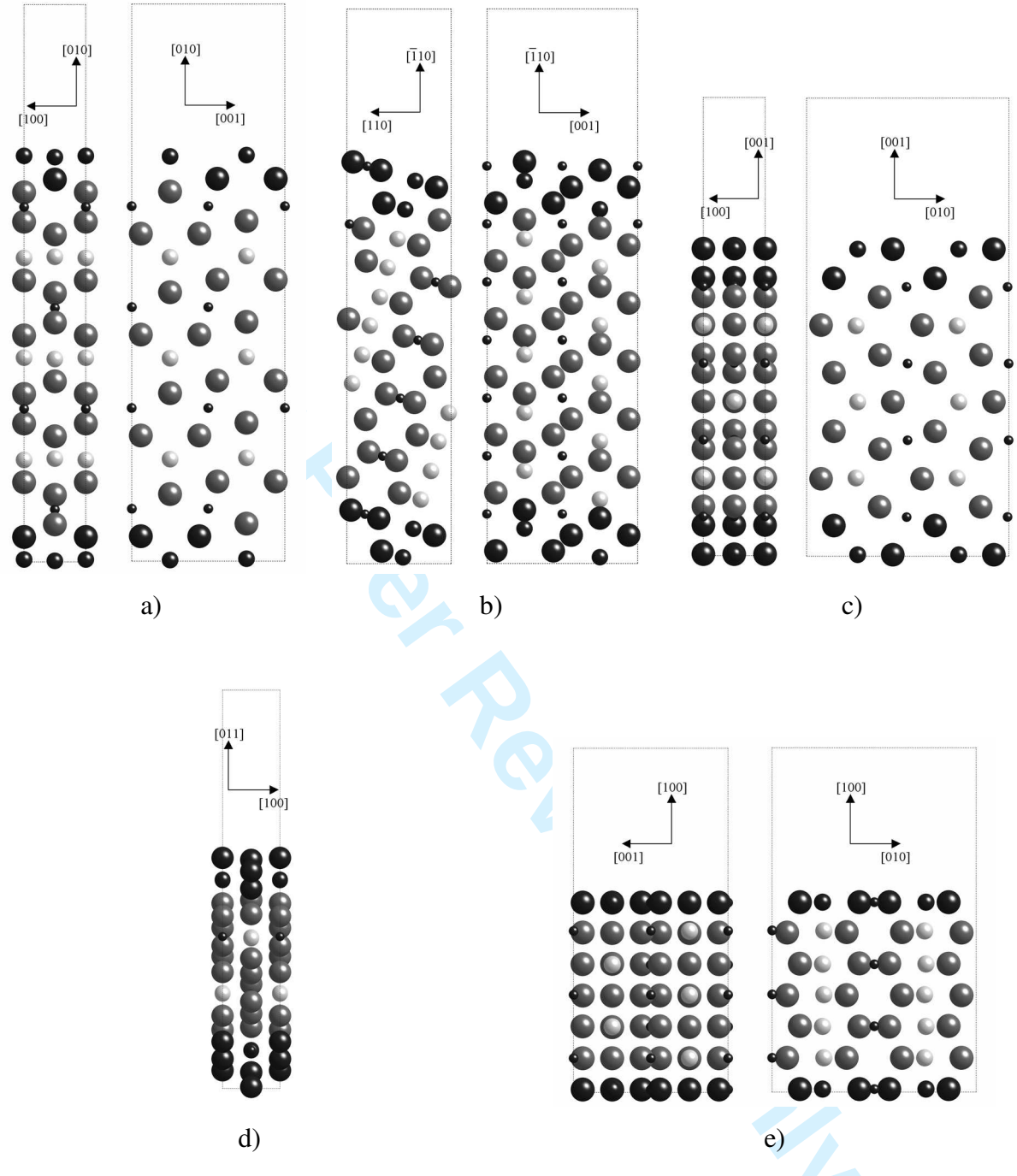
[010]
[100]
[010]
[001]
[$\bar{1}$10]
[110]
[$\bar{1}$10]
[001]
[001]
[100]
[001]
[010]
a)
b)
c)
[011]
[100]
[100]
[001]
[100]
[010]
d)
e)

Figure 2

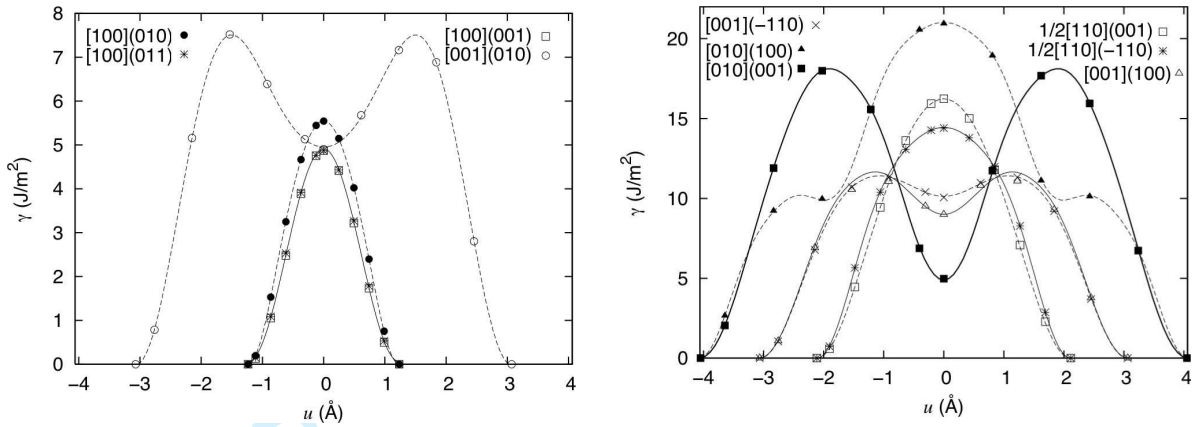

(a) (b)

Figure 3

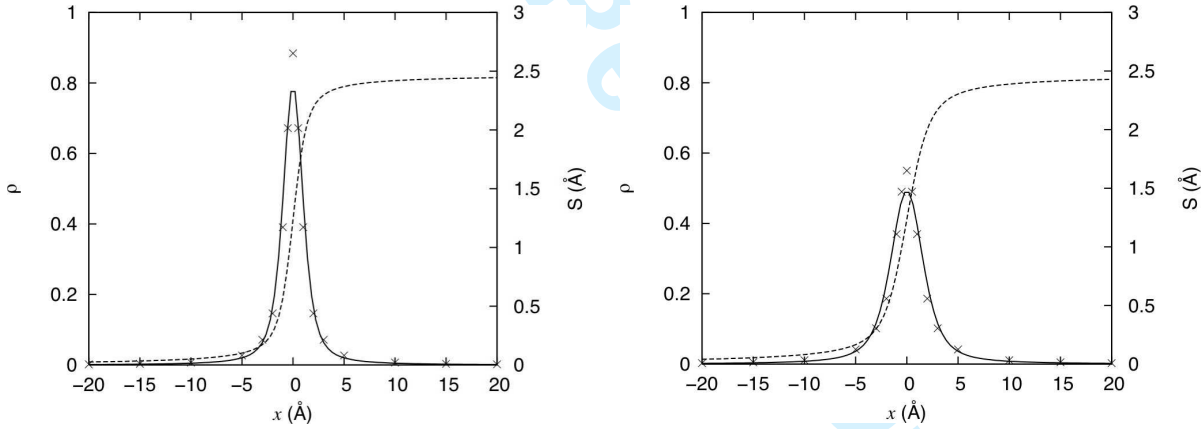

(a) (b)

Figure 4

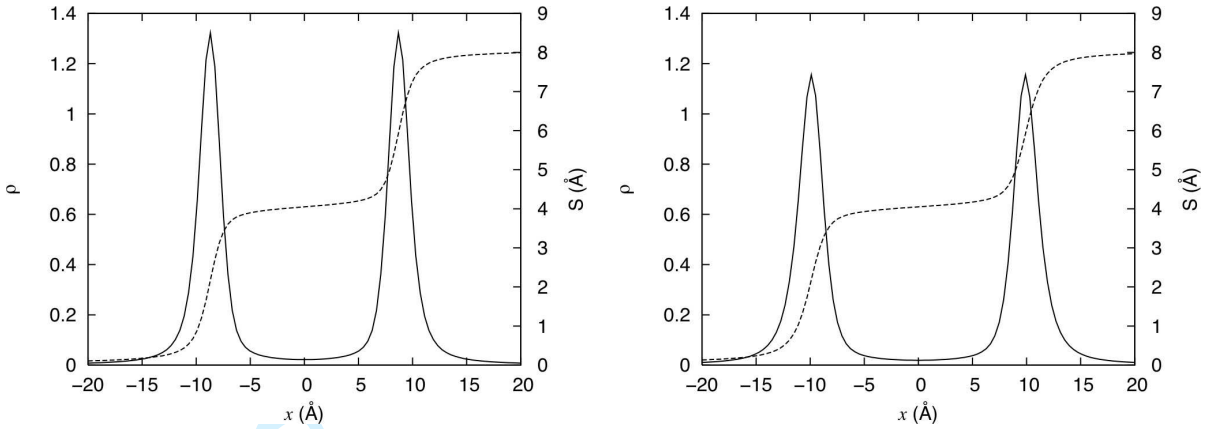

(a) (b)

Figure 5

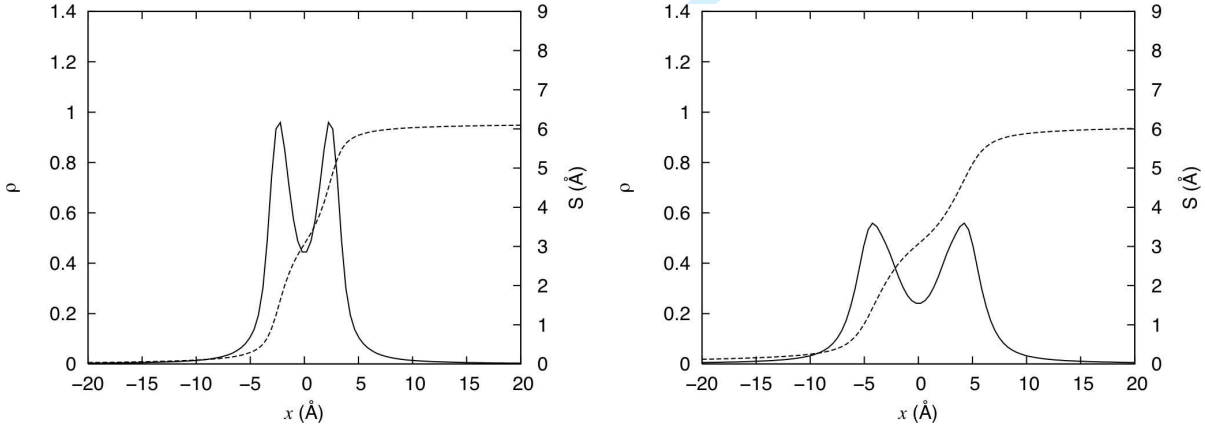

(a) (b)

Figure 6

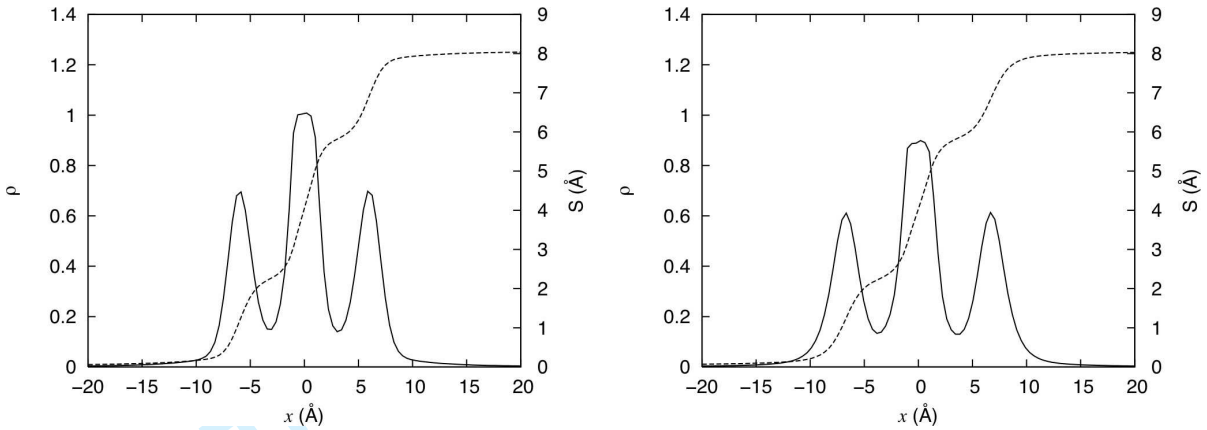

(a) (b)

Figure 7